Batteries & Supercaps

Research Article
doi.org/10.1002/batt.202400745

Chemistry
Europe
European Chemical
Societies Publishing

www.batteries-supercaps.org

Acoustic Particle Patterning Aided by Phase-inversion for Efficient Structuring of Low-Tortuosity Battery Electrodes

Yifan Zhang,[a] M Shahriar,[a] and Shan Hu*[a]

Texturing the battery electrode to create low-tortuosity ordered structures can significantly improve the sluggish mass transport in thick electrodes (areal mass loading > 20 mg/cm^2) during the energy storage electrochemical reactions. In this work, we presented an efficient and effective method to regulate the electrode structure by creating aligned channels throughout the thickness of the electrode. The method combines acoustic manipulation of particles and nonsolvent induced phase inversion and is highly compatible with a wide range of materials used in various battery chemistries. The textured electrodes show better structural integrity compared to electrodes of similar mass loading made with acoustic patterning only and with conventional solution casting. Compared with electrodes made with phase inversion only, it exhibits lower tortuosity, enhanced ion transport/kinetics, better rate capability and cyclic stability.

Introduction

Lithium-ion battery (LIB) is a key enabler for electric vehicles (EVs). Although LIB technology has come a long way since it was first invented in 1979, there is a concerted effort around the world to further increase its energy density such that EVs users can have less range anxiety.[1–6] Meanwhile, tremendous efforts are also placed on driving down the cost of lithium-ion batteries to make EVs more economical for wider market acceptance. Besides developing new cathode and anode chemistries, a straightforward way towards high-energy-density and low-cost LIB is to use thick electrodes (i.e. electrodes with high areal mass loading). This is because using thick electrodes effectively reduces the mass and volume percentage of inactive components in battery cells. Theoretically, this should effectively increase the specific capacity and energy density at the cell level, while lowering the cell cost due to reduced inactive material usage and manufacturing cost.[7–10] However, thick electrodes suffer significant capacity loss as charge/discharge rates increase. Such a performance loss is especially severe for electrodes with high tortuosity. Tortuosity quantifies the average path length an ion traverses from the bulk electrolyte to the reaction site at the electrode-electrolyte interface. Under high charge/discharge rates, ions in high-tortuosity electrodes only reach the active materials nearest to the bulk electrolyte, resulting in a limited portion of the materials participating in the energy storage reaction. This significantly restricts both the

capacity and energy density and negates the benefits of using thick electrodes.[11–15] Various methods have been developed to reduce the tortuosity of thick electrodes by constructing highly ordered structures in the electrodes in recent years.[16–38] Among these methods, acoustic particle pattering has unique advantages, because it can be applied to a broad range of electrode materials for different battery chemistries without incurring material loss/damage or adding foreign materials to the electrodes.[39–42] During acoustic particle patterning of battery electrodes (Figure 1 (a–b)), piezoelectric actuators are first coupled to the current collector coated with wet film of slurry. When a voltage of certain frequency is applied to the actuators, the vibrating current collector exerts acoustic radiation force on the solid particles (i.e. active material and carbon additive). This force moves the particles away from the acoustic antinodes (regions with the highest acoustic pressure) and concentrates them at the acoustic nodes (regions with the lowest acoustic pressure). After drying, the acoustically patterned electrodes have evenly spaced trenches at the antinode locations, which serves as low-tortuosity ion transport pathways.

Despite unique advantages, the acoustic particle patterning of battery electrodes faces one major challenge. After acoustic patterning is achieved in the wet electrode, voltage must continue to be supplied to the piezo actuators during the subsequent drying process (> 1 hour). Otherwise, the particles' motion during the drying process would re-randomize the spatial distribution of particles, leading to partial or complete disappearance of the trenches in the final dried electrodes. This adds extra energy consumption to the electrode manufacturing process. To be more energy-efficient, a mechanism is needed to "freeze" the solid particles in place after acoustic patterning step, so there is no need to sustain the vibration of the current collector during the drying step to counteract the forces that drives the redistribution of particles.

To overcome the challenge and enable efficient, effective patterning of thick battery electrodes, herein an integrated solution that combines acoustic particle patterning (AP) with phase inversion (PI), termed APPI, is investigated. As shown in

[a] Y. Zhang, M Shahriar, S. Hu
Department of Mechanical Engineering, Iowa State University, Ames, Iowa, 50014, USA
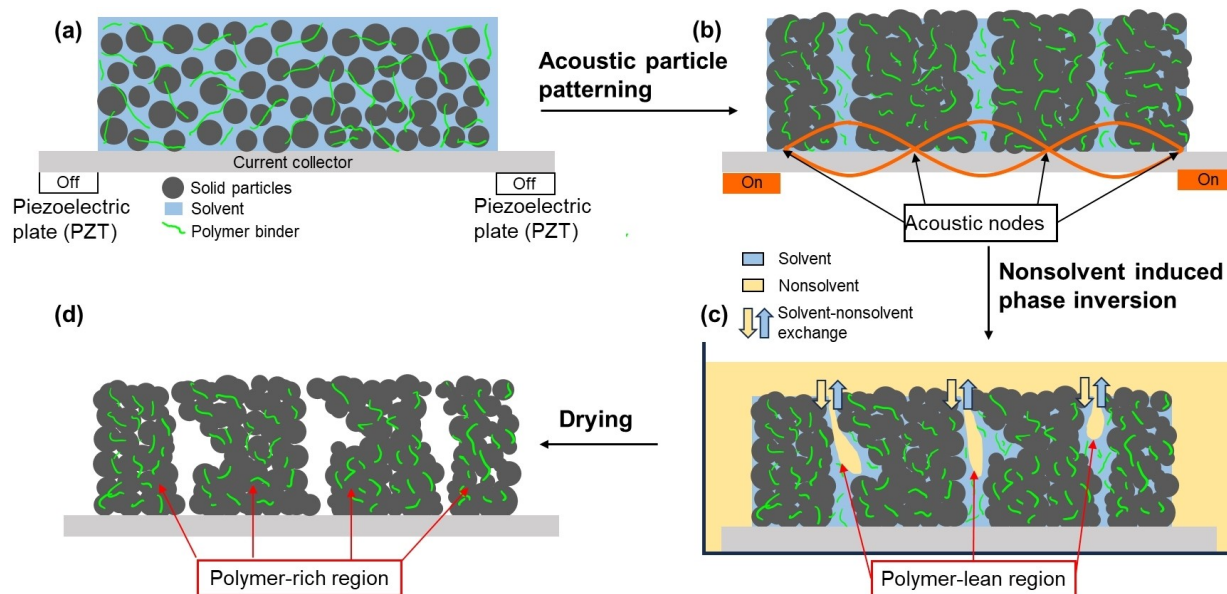E-mail: shanhu@iastate.edu

Figure 1. Schematic of the acoustic pattering process aided by phase inversion (APPI) for structuring low-tortuosity battery electrodes. (a) Wet electrode coated on current collector is placed on top of piezo electric actuators. (b) The piezo electric actuators are activated for acoustic patterning of electrode particles. (c) The acoustically patterned wet electrode is immersed into a non-solvent bath, where the wet electrode phase separates into polymer-lean and polymer-rich regions. (d) After phase inversion, wet electrode is taken out of the bath and dried. Polymer-rich regions become the matrix of the electrode and polymer-lean regions become the pores inside the electrode.

Figure 1, the wet electrode that contains solid particles (active materials and carbon additives), polymer binder and solvent is first subjected to acoustic particle patterning, which generates through-thickness trenches in the wet electrode. Subsequently, the patterned electrode is immersed in a bath filled with non-solvent for the polymer binder. Because of concentration gradient, nonsolvent continues to diffuse into the wet electrode and solvent diffuses out. The low solubility of polymer in nonsolvent results in aggregation of the polymer and the polymer-binding solid particles, which solidifies them into polymer-rich regions. This serves to preserve the trench created by the previous acoustic particle patterning step and waives the need to continuously applying acoustic field to counteract the particles' motion that can re-randomized the particle distribution. Furthermore, immersion of wet electrode in the nonsolvent bath generates low-tortuosity porous structures in the electrode in addition to the trenches created by the acoustic field. This is because of non-solvent induced phase separation, in which the diffusion of nonsolvent into the electrode causes it to separate into polymer-rich and polymer-lean phases. After drying, the polymer-lean phase becomes additional pores in the electrodes.

Results and Discussion

The fabrication process of APPI-LFP and PI-LFP electrodes are illustrated in Figure 1. After coating the slurry on the aluminum foil, the APPI-LFP electrode sample was structured by the acoustic-field patterning firstly then immersed in the water coagulation bath for phase-inversion process while the acous-tic-field patterning step was not applied to fabricate the PI-LFP electrode. The acoustic-field patterning process aids the solid materials to concentrate on the nodes of the standing acoustic waves established on the current collector. The concentration of solid materials at the nodes increases the viscosity of slurry in these regions and decreases the slurry viscosity elsewhere in the wet electrode. When the acoustically patterned electrodes were immersed in the nonsolvent bath, concentration gradients of solvent (NMP) and nonsolvent (DI water) drives their exchange out and into the electrode respectively. Particularly, the exchange is faster in the acoustic antinode regions where solid materials were lean, due to lower viscosity. As a result of the solvent-nonsolvent exchange and the low solubility of the polymer binder in the nonsolvent, polymer and polymer-binding solid particles further aggregate and consolidate in the acoustic nodal areas where they were previously concentrated by the acoustic field. The mobility of the solid particles becomes restricted inside the consolidated electrodes, which aids the fixation of particles' spatial distribution to form low-tortuosity structures and reduces re-randomization of particles' distribution during the subsequent drying step. Therefore, after the drying, the APPI-LFP electrode has a series of evenly spaced channels inside the electrode through the thickness, as shown in Figure 2a.

For the PI-LFP electrode, there are no pre-structured low-viscosity and high-viscosity regions in the homogeneous wet electrode before immersing it into the nonsolvent bath. Hence the solvent-nonsolvent exchange starts at random locations and proceeds into the wet electrode following a random path. After the phase inversion and drying steps, the PI-LFP electrode
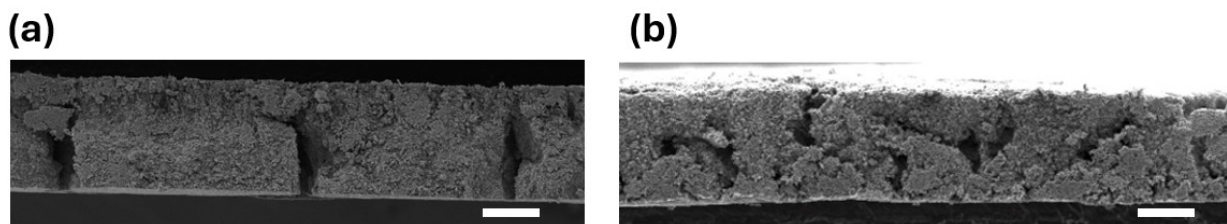
Batteries & Supercaps

Research Article
doi.org/10.1002/batt.202400745

Chemistry Europe
European Chemical
Societies Publishing

Figure 2. Scanning electron microscopy (SEM) of the cross-sectional area of (a) APPI-LFP electrode and (b) PI-LFP electrode with areal mass loading of 29.5 mg/cm^2. Vertical channels, which are separated by almost equal distance, were generated in the APPI-LFP electrode, while such feature is not observed in the PI-LFP electrode. Scale bar: 200 μm.

shows random porous structures without aligned channels along the thickness direction, as demonstrated in Figure 2b.

On the other hand, the uniform distribution of PVDF polymer binder is crucial for the electrode to maintain structural integrity and mechanical properties for its electrochemical performance. According to Figure S1 and S2, the element distribution around one of the channels was evaluated by the energy dispersive X-ray spectroscopy (EDS), which demonstrates that fluorine is homogeneous in the regions where electrochemically active materials are located.

The evenly spaced and aligned channels built through the thickness of the APPI-LFP electrode are less tortuous than the random porous structures of the PI-LFP electrode, hence it is expected that the APPI-LFP electrode has shorter diffusion pathway of lithium-ions and more favorable electrochemical performance than the PI-LFP electrode. For electrochemical performance, cyclic voltammetry (CV) and electrochemical impedance spectroscopy (EIS) were measured to assess the kinetics and compare the lithium-ion diffusion behavior between APPI-LFP and PI-LFP electrodes with similar areal mass loading of 29.5 mg/cm^2. It is worth mentioning that the electrodes with same areal mass loading fabricated by only acoustic-field patterning (AP-LFP) and solution casting (SC-LFP) method were not able to maintain an intact structure due to severe cracking on the electrodes after drying as shown in Figure S3. Such cracking was not observed in APPI-LFP and PI-LFP electrodes after drying, likely due to stronger cohesion

between particles caused by the consolidation of solid contents during phase inversion. AP-LFP and SC-LFP electrodes (Figure S4) without cracking were fabricated at lower areal mass loadings of 12.9 and 12.2 mg/cm^2 respectively, for comparison with the APPI-LFP and PI-LFP electrodes with areal mass loading of 29.5 mg/cm^2. Note that even if the wet AP-LFP electrode shows line patterns generated by acoustic-field patterning (Figure S4a), these line patterns disappeared in the dried AP-LFP electrode (no trenches along the thickness direction were observed in the dried electrode shown in Figure S4b and S4d. This demonstrates the need to use the phase inversion step following acoustic patterning to preserve the acoustically generated patterns.

Figure 3a demonstrates the Nyquist plots of all four electrodes. According to the equivalent circuit shown in the inset of Figure 3a, the first and second intercept of the semi-circle between the Nyquist plot and the Re(Z) axis represent the internal resistance (R_u) and charge-transfer resistance (R_{ct}) at the high- and mid-frequency region. On the other hand, the Warburg impedance (W), which is attributed to mass transport, is estimated by the measurement of low-frequency region.[43] Upon fitting of the semi-circle, APPI-LFP electrode shows the lowest R_{ct} of 20.9 Ω, followed by PI-LFP of 68.2 Ω, AP-LFP of 247.8 Ω and SC-LFP of 283.5 Ω. Besides, the data points from the low-frequency regions were selected, and values of real impedance corresponding to each point are plotted with the inverse square root of angular frequency ($\omega^{-1/2}$) as Figure 3b
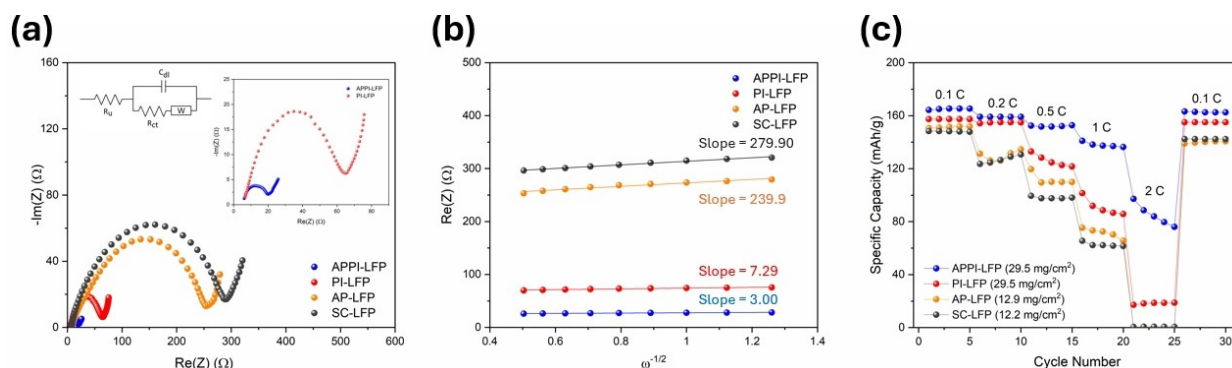

Figure 3. (a) Electrochemical impedance spectroscopy (EIS) at frequency between 1 MHz and 0.1 Hz with half cells using APPI-LFP, PI-LFP, AP-LFP or SC-LFP as working electrode and lithium metal as counter electrode (insets: equivalent circuit for EIS and zoomed in Nyquist plots of APPI-LFP and PI-LFP electrodes). (b) Real impedance versus $\omega^{-1/2}$ plot taken from EIS data in low-frequency range. in EIS measurements. (c) Rate performance comparison of all four electrodes from 0.1 C to 2 C.

Batteries & Supercaps

Research Article
doi.org/10.1002/batt.202400745

Chemistry Europe
European Chemical
Societies Publishing

shows. Based on the relation between Warburg coefficient (σ) and lithium-ion diffusion (D_{Li^+}), the estimated lithium-ion diffusion of APPI-LFP electrode is 3.08×10^{-9} cm^2/s, much higher than PI-LFP (5.22×10^{-10} cm^2/s), AP-LFP (4.82×10^{-13} cm^2/s) and SC-LFP (3.54×10^{-13} cm^2/s) electrodes. Detailed process of estimating lithium-ion diffusion from the EIS is provided in Supplementary Information. According to these two results, the architecture formed by phase-inversion process combined with the acoustic-field patterning of the solid material can further facilitate the ion transport in the electrode compared to the ones fabricated by only phase-inversion, by only acoustic-field patterning and by only slurry casting.

As for galvanostatic cycling performance, the half cells with LFP electrode as working electrode were tested at various rates ranging from 0.1 C to 2 C with the results shown in Figure 3c. When cycling at low current density (<0.5 C), all four electrodes show no significant difference in terms of specific discharge capacity. At high C-rates (≥ 0.5 C), however, APPI-LFP electrode demonstrates considerable advantage with 152.5, 141.0 and 97.1 mAh/g at 0.5 C, 1 C and 2 C discharge, respectively, over PI-LFP electrode (133.0, 101.5, 18.7 mAh/g at 0.5 C, 1 C and 2 C,

respectively). Both APPI-LFP and PI-LFP electrodes show higher specific capacity than AP-LFP and SC-LFP electrodes at high C-rates even though the latter two electrodes have much lower areal mass loading. Since APPI-LFP and PI-LFP electrodes showed better performances in the EIS and rate capability tests, more detailed electrochemical characterization of these two electrodes were conducted. From the voltage profiles throughout the C-rates in Figure S5, APPI-LFP electrode also exhibits a lower overpotential of charge and discharge process compared to PI-LFP electrode.

Cyclic voltammograms of APPI-LFP and PI-LFP electrodes at scan rate of 0.1 mV/s are shown in Figure 4a. Compared to PI-LFP electrode, the APPI-LFP electrode exhibits larger peak current at both anodic and cathodic regions as well as lower overpotential based on less distance between peaks, which indicates better kinetics of the electrode. Furthermore, DC-polarization was applied to quantify the tortuosity of structure inside the electrodes. As illustrated in Figure 4b, the symmetric cells were built with the free-standing LFP electrode placed in-between two lithium metal disks with one layer of polymer separator on each side of LFP electrode. A similar configuration
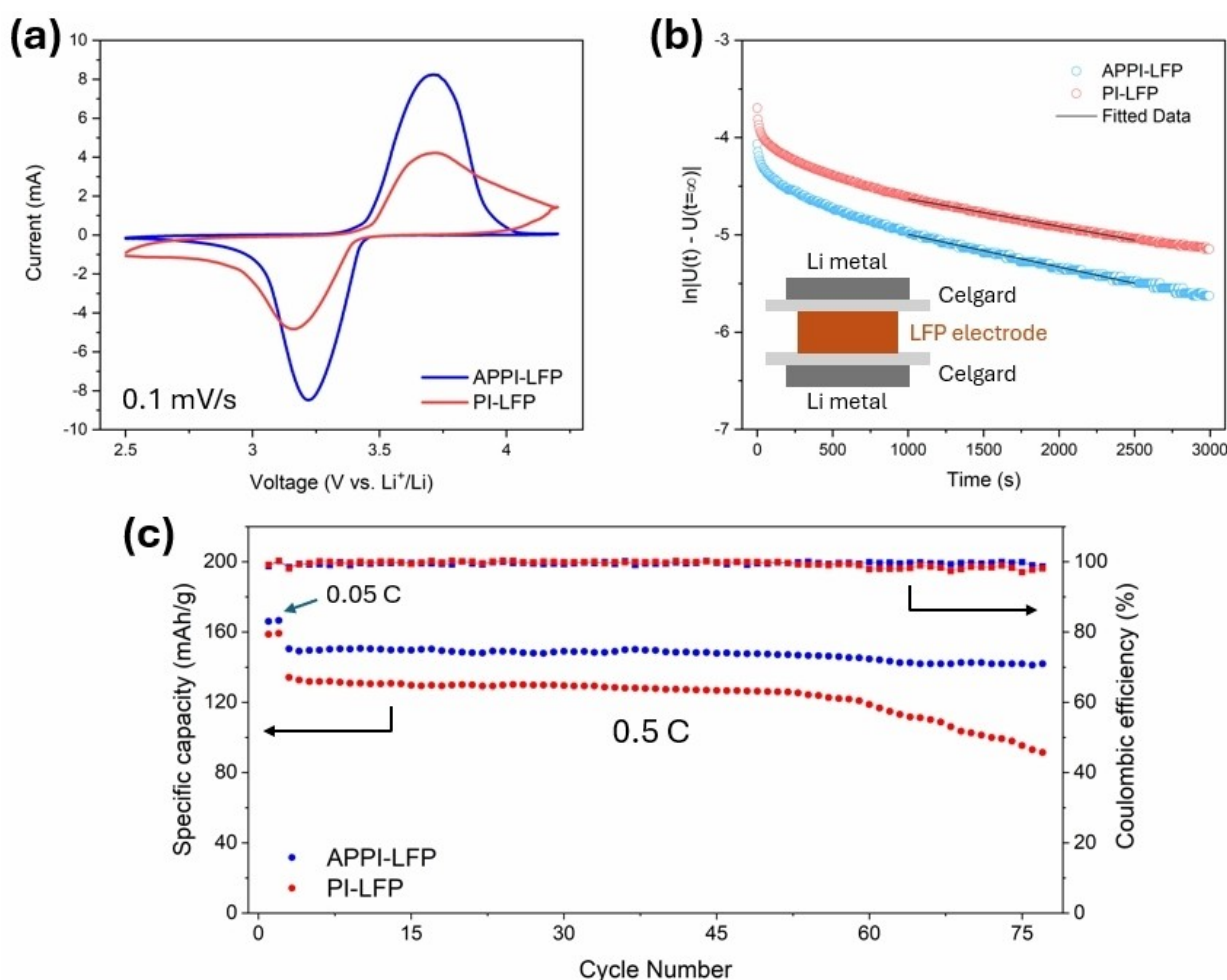

Figure 4. Electrochemical testing results of APPI-LFP and PI-LFP electrodes. (a) cyclic voltammetry at 0.1 mV/s with half cells using APPI-LFP or PI-LFP as working electrode and lithium metal as counter electrode. (b) DC-polarization data measured with Li|Celgard|APPI-LFP|Celgard|Li and Li|Celgard|PI-LFP|Celgard|Li symmetric cells. (c) Discharge capacity and coulombic efficiency for 75 cycles for both electrodes at 0.5 C cycling, including 2 formation cycles at 0.05 C.

Batteries & Supercaps

Research Article
doi.org/10.1002/batt.202400745

Chemistry
Europe

European Chemical
Societies Publishing

was used to measure the diffusivity of electrolyte by replacing the LFP electrode with PTFE O-ring as spacer (Figure S6). At the beginning of measurement, ion concentration gradient was formed by a small polarization current (10 μA). Then the cells turned into relaxation and a steady voltage was achieved after a certain duration. The linear part of the curve originated from the DC-polarization test can be fitted as Figure 4b illustrates to estimate the ion diffusivity in the layer sandwiched between the two lithium metal plates. Detailed estimation method is given in Supplementary Information. Based on the estimation, the intrinsic diffusivity of the electrolyte (D_0) that was used in half-cell building was 6.67×10^{-7} cm^2/s, which is close to the values in related literature.[44] On the other hand, the effective diffusivity (D_{eff}) in symmetric cells with APPI-LFP and PI-LFP electrode was calculated from the cells' DC-polarization data as listed in Table S2. Based on the relation between tortuosity with porosity (ε), intrinsic and effective diffusivity, $D_{eff} = \varepsilon D_0 / \tau$, the estimated tortuosity (τ) of APPI-LFP and PI-LFP electrode is 7.77 and 11.8, respectively, which confirms that acoustic-field patterning combined with the phase-inversion process generates a less tortuous electrode. This result proves that lithium-ion diffusion is boosted for the APPI-LFP electrode compared to PI-LFP electrode. Additionally, APPI-LFP electrode demonstrates an excellent capacity retention of 94.3% after 75 cycles at 0.5 C charge and discharge, while PI-LFP electrode only maintained 68.2% of retention with fast drop of capacity after 50 cycles, as shown in Figure 4c. From the voltage profiles in various cycles illustrated in Figure S7, the growth of overpotential is lower for APPI-LFP electrode than for PI-LFP electrode. Both results indicate that the enhanced diffusion in APPI-LFP electrode aids the improvement of long-term cycling stability.

Conclusions

In conclusion, we demonstrate the acoustic pattering process aided by phase inversion (APPI) for reducing the tortuosity of thick LFP electrode with high areal mass loading (>20 mg/cm^2). In the APPI process, acoustic particle patterning is mainly responsible for generating aligned channels in the thickness direction at the acoustic anti-node locations, whereas the PI step helps to further aggregate and consolidate the solid particles previously concentrated at the acoustic nodes by the acoustic field. The added PI step restricts particles' motion that could eradicate the acoustically generated patterns. Hence it waives the need to keep applying acoustic actuation to the electrode during the drying process. The as-fabricated APPI-LFP electrode exhibits aligned and evenly spaced channels which serve as low-tortuosity ion diffusion pathways. On the other hand, LFP electrode processed by phase inversion only (PI-LFP) shows randomly spaced and crooked channels. It is worth mentioning that LFP electrodes fabricated by acoustic particle patterning (AP-LFP) and conventional solution casting (SC-LFP) both show severe cracking at the same areal mass loading as APPI-LFP and PI-LFP electrodes. Even though the cracking in AP-LFP and SC-LFP electrodes was mitigated by reducing the areal mass loading, the AP-LFP and SC-LFP electrodes with low

mass loading showed inferior electrochemical performances compared to that of APPI-LFP electrode with much higher mass loading. Furthermore, tortuosity measurement confirms that the APPI-LFP electrode has much lower tortuosity than PI-LFP electrode. As a result, lithium-ion diffusivity is higher in APPI-LFP electrode than in PI-LFP electrode. In addition, APPI-LFP electrode shows advantageous charge transfer kinetics and lower overpotentials in electrochemical tests. These advantages help APPI-LFP electrode achieve better rate performance and cycling stability in the battery performance tests with LFP—Li half cells. This work advances the acoustic particle patterning-based method for fabricating low-tortuosity battery electrode with high areal mass loading. It allows the acoustic structuring of thick electrode without severe cracking and greatly increases the energy-efficiency of this method by removing the need to continuously applying acoustic energy to the patterned electrode during the lengthy drying process.

Experiments

Fabrication of LFP electrodes

In this work, prior to the fabrication of all types of LFP electrode, polyvinylidene fluoride (PVDF) (M_w ~180,000 g/mol, Sigma Aldrich) polymer solution was prepared with N-methyl-2-pyrrolidone (NMP) (Sigma Aldrich) as solvent with 10 wt.% of polymer concentration. After that, LFP powder (D50~1.5 μm, MSE Supplies) and acetylene black (AB) (100% compressed, Alfa Aesar) were added into PVDF solution with solid material ratio as LFP: PVDF: AB = 80: 15: 5, followed by mixing in THINKY mixer (AR-100) at 400 rpm for 5 minutes for a homogeneous slurry with solid materials uniformly dispersed.

For the preparation of the APPI-LFP electrode, the slurry was first coated on a 15-μm thick aluminum foil (MTI Corporation) with the thickness of coating layer of 300-um controlled by doctor blade. To create aligned structures by acoustic-field patterning, the as-coated aluminum foil was attached to the piezoelectric actuator (20×15×1.4 mm 1.5 MHz, Steiner & Martins, Inc.) with vacuum grease in-between to enhance the attachment. A sinusoidal voltage with frequency and peak-to-peak amplitude of 80 kHz and 120 V$_{pp}$ respectively was applied to the piezoelectric actuator by an arbitrary function generator (DG1022, Rigol Technologies, Inc) and a signal amplifier (2350 Precision Power Amplifier, TEGAM Inc.). After 15 minutes of acoustic-field patterning, the electrode was immersed in the deionized water (DI water) non-solvent bath for 1 hour of phase-inversion process. Finally, the free-standing electrode was initially dried on hot plate at 60 °C and transferred into vacuum oven to dry overnight before characterization and electrochemical tests. For comparison with APPI-LFP electrode, three types of electrodes were prepared by phase-inversion process (PI-LFP), acoustic-field patterning (AP-LFP) and solution casting (SC-LFP). PI-LFP was prepared using the same phase inversion step as APPI-LFP electrode but skipping the first acoustic-field patterning step. The AP-LFP electrode was prepared using the same acoustic-field patterning step as APPI-LFP electrode, however the phase inversion step was skipped. The SC-LFP electrode was prepared by simply coating the slurry on the current collector followed by drying. PI-LFP, AP-LFP and SC-LFP electrodes were all subjected to the same drying procedure as the APPI-LFP electrode. During drying no acoustic field was applied to any electrodes.

Batteries & Supercaps

Research Article
doi.org/10.1002/batt.202400745

Chemistry
Europe
European Chemical
Societies Publishing

Characterization of Morphology

The morphology and element distribution of the cross-sectional area of electrodes were characterized by scanning electron microscopy (SEM) and energy dispersive X-ray spectroscopy (EDS) (FEI Inspect F50).

Electrochemical Tests

Cell assembly: The fabricated LFP electrodes were punched into 12-mm disk before the cell assembly. The CR2032 coin cells were built with LFP electrode and one piece of lithium metal disk (16-mm diameter) as working and counter electrode, respectively, for half-cell testing. Sandwiched between the two electrodes was a piece of Celgard 2400 polymer separator soaked with electrolyte of 1 M $LiPF_6$ in ethylene carbonate (EC) and diethyl carbonate (DEC) with 1:1 volumetric ratio and 2 wt.% of vinylene carbonate (VC) as additive. All coin cells were built inside the glovebox filled with argon (oxygen and moisture level less than 3 ppm).

Electrochemical measurement for half-cells: Electrochemical impedance spectroscopy (EIS) was measured at frequency between 1 MHz and 0.1 Hz with AC voltage of 200 mV on an electrochemical working station (Gamry Reference 3000). Cyclic voltammetry was scanned between 2.5 V and 4.2 V vs. Li^+/Li at 0.1 mV/s. For galvanostatic tests, the cells were charged and discharged for 2 cycles at 0.05 C (1 C = 170 mA/g) rate as formation cycles before rate performance or long-term cycling at various C-rates between 2.5 V and 4.0 V.

DC-polarization test: Symmetric cells were built with lithium metal chip as electrode with one piece of Celgard 2400 polymer separator on each electrode side, sandwiching the one 12-mm disk of APPI-LFP or PI-LFP electrode in-between. The electrolyte used is the same as the one in half-cell assembly. On the other hand, the LFP electrode was replaced by one piece of PTFE O-ring (1.63-mm thick, McMaster) as a spacer in between the lithium metal disks separated by Celgard 2400 polymer separator on each side for the diffusivity measurement of electrolyte. The cells for DC-polarization were rested for 12 hours for fully wetting of electrode before a polarization current of 0.01 mA was applied for 2 hours. After polarization, the current was cut off to allow the cells to rest until $dU/dt < 0.1$ mV/h.

Conflict of Interests

The authors declare no conflict of interest.

Data Availability Statement

The data that support the findings of this study are available from the corresponding author upon reasonable request.

Keywords: Microstructure · Tortuosity · Acoustic Patterning · Phase Inversion · Mass Transport

[1] G. Zubi, R. Dufo-López, M. Carvalho, G. Pasaoglu, *Renewable Sustainable Energy Rev.* **2018**, *89*, 292.
[2] J. B. Goodenough, K.-S. Park, *J. Am. Chem. Soc.* **2013**, *135*, 1167.
[3] T. Kim, W. Song, D.-Y. Son, L. K. Ono, Y. Qi, *J. Mater. Chem. A* **2019**, *7*, 2942.
[4] M. Armand, P. Axmann, D. Bresser, M. Copley, K. Edström, C. Ekberg, D. Guyomard, B. Lestriez, P. Novák, M. Petranikova, W. Porcher, S. Trabesinger, M. Wohlfahrt-Mehrens, H. Zhang, *J. Power Sources* **2020**, *479*, 228708.
[5] J. Li, J. Fleetwood, W. B. Hawley, W. Kays, *Chem. Rev.* **2021**, *122*, 903.
[6] N. Nitta, F. Wu, J. T. Lee, G. Yushin, *Mater. Today* **2014**, *18*, 252.
[7] Y. Kuang, C. Chen, D. Kirsch, L. Hu, *Adv. Energy Mater.* **2019**, *9*, 1901457.
[8] M. Singh, J. Kaiser, H. Hahn, *J. Electrochem. Soc.* **2015**, *162*, A1196.
[9] D. J. Arnot, K. S. Mayilvahanan, Z. Hui, K. J. Takeuchi, A. C. Marschilok, D. C. Bock, L. Wang, A. C. West, E. S. Takeuchi, *Acc. Mater. Res.* **2022**, *3*, 472.
[10] Z. Wang, C. Dai, K. Chen, Y. Wang, Q. Liu, Y. Liu, B. Ma, L. Mi, W. Mao, *J. Power Sources* **2022**, *551*, 232176.
[11] H. Zheng, J. Li, X. Song, G. Liu, V. S. Battaglia, *Electrochim. Acta* **2012**, *71*, 258.
[12] Y. Chen, B. Zhao, Y. Yang, A. Cao, *Adv. Energy Mater.* **2022**, *12*, 2201834.
[13] Z. Du, D. L. Wood, C. Daniel, S. Kalnaus, J. Li, *J. Appl. Electrochem.* **2017**, *47*, 405.
[14] M. J. Lain, E. Kendrick, *J. Power Sources* **2021**, *493*, 229690.
[15] I. V. Thorat, D. E. Stephenson, N. A. Zacharias, K. Zaghib, J. N. Harb, D. R. Wheeler, *J. Power Sources* **2008**, *188*, 592.
[16] Z. Song, P. Zhu, W. Pfleging, J. Sun, *Nanomaterials* **2021**, *11*, 2962.
[17] Y. Zhang, M. Shahriar, S. Hu, *J. Mater. Chem. A* **2023**, *11*, 11849.
[18] H. Ren, Y. Wang, D. Cao, W. Gedney, T. Ji, X. Sun, H. Zhu, *Energy Environ. Mater.* **2023**, *6*, e12584.
[19] H. Wang, J. Li, Z. Miao, K. Huang, Y. Liao, X. Xu, J. Meng, Z. Li, Y. Huang, *ACS Appl. Mater. Interfaces* **2023**, *15*, 26824.
[20] Y. Wang, Y. Zhang, D. Cao, T. Ji, H. Ren, G. Wang, Q. Wu, H. Zhu, *Small Methods* **2023**, *7*, 2201344.
[21] J. Wu, Z. Ju, X. Zhang, K. J. Takeuchi, A. C. Marschilok, E. S. Takeuchi, G. Yu, *Nano Lett.* **2021**, *21*, 9339.
[22] J. Wu, Z. Ju, X. Zhang, C. Quilty, K. J. Takeuchi, D. C. Bock, A. C. Marschilok, E. S. Takeuchi, G. Yu, *ACS Nano* **2021**, *15*, 19109.
[23] J. Wang, M. Wang, N. Ren, J. Dong, Y. Li, C. Chen, *Energy Storage Mater.* **2021**, *39*, 287.
[24] J. Wu, Z. Ju, X. Zhang, X. Xu, K. J. Takeuchi, A. C. Marschilok, E. S. Takeuchi, G. Yu, *ACS Nano* **2022**, *16*, 4805.
[25] S. Yang, C. Zhou, Q. Wang, B. Chen, Y. Zhao, B. Guo, Z. Zhang, X. Gao, R. Chowdhury, H. Wang, C. Lai, N. P. Brandon, B. Wu, X. Liu, *Energy Environ. Mater.* **2021**, *5*, 1332.
[26] L. Li, R. M. Erb, J. Wang, J. Wang, Y. Chiang, *Adv. Energy Mater.* **2018**, *9*, 1802472.
[27] X. Zhang, Z. Hui, S. King, L. Wang, Z. Ju, J. Wu, K. J. Takeuchi, A. C. Marschilok, A. C. West, E. S. Takeuchi, G. Yu, *Nano Lett.* **2021**, *21*, 5896.
[28] X. Zhang, Z. Ju, L. M. Housel, L. Wang, Y. Zhu, G. Singh, N. Sadique, K. J. Takeuchi, E. S. Takeuchi, A. C. Marschilok, G. Yu, *Nano Lett.* **2019**, *19*, 8255.
[29] Y. Guo, Y. Jiang, Q. Zhang, D. Wan, C. Huang, *J. Power Sources* **2021**, *506*, 230052.
[30] D. Dang, Y. Wang, S. Gao, Y.-T. Cheng, *Carbon* **2019**, *159*, 133.
[31] K.-H. Chen, M. J. Namkoong, V. Goel, C. Yang, S. Kazemiabnavi, S. M. Mortuza, E. Kazyak, J. Mazumder, K. Thornton, J. Sakamoto, N. P. Dasgupta, *J. Power Sources* **2020**, *471*, 228475.
[32] J. S. Sander, R. M. Erb, L. Li, A. Gurijala, Y.-m. Chiang, *Nat. Energy* **2016**, *1*, 16099.
[33] B. Delattre, R. Amin, J. Sander, J. De Coninck, A. P. Tomsia, Y.-M. Chiang, *J. Electrochem. Soc.* **2018**, *165*, A388.
[34] C. Huang, M. Dontigny, K. Zaghib, P. S. Grant, *J. Mater. Chem. A* **2019**, *7*, 21421.

Batteries & Supercaps

Research Article
doi.org/10.1002/batt.202400745

**Chemistry
Europe**
European Chemical
Societies Publishing

[35] Y. Zhang, Y. Xiao, L. Chen, S. Hu, *J. Mater. Chem. A* **2024**, *12*, 16537.

[36] R. He, C. Cai, S. Li, S. Cheng, J. Xie, *Small* **2024**, *20*, 2311044.

[37] S. Li, G. Tian, R. Xiong, R. He, S. Chen, H. Zhou, Y. Wu, Z. Han, C. Yu, S. Cheng, J. Xie, *Energy Storage Mater.* **2022**, *46*, 443.

[38] R. He, G. Tian, S. Li, Z. Han, W. Zhong, S. Cheng, J. Xie, *Nano Lett.* **2022**, *22*, 2429.

[39] P. Zhang, H. Bachman, A. Ozcelik, T. J. Huang, *Annu. Rev. Anal. Chem.* **2020**, *13*, 17–43.

[40] X. Ding, P. Li, S.-C. S. Lin, Z. S. Stratton, N. Nama, F. Guo, D. Slotcavage, X. Mao, J. Shi, F. Costanzo, T. J. Huang, *Lab Chip* **2013**, *13*, 3626.

[41] K. Melde, E. Choi, Z. Wu, S. Palagi, T. Qiu, P. Fischer, *Adv. Mater.* **2018**, *30*, 1704507.

[42] L. Lu, X. Tang, S. Hu, Y. Pan, *3D Print. Addit. Manuf.* **2018**, *5*, 151.

[43] A. Ch Lazanas, M. I. Prodromidis, *ACS Meas. Sci. Au* **2023**, *3*, 162.

[44] Z. Feng, K. Higa, K. S. Han, V. Srinivasan, *J. Electrochem. Soc.* **2017**, *164*, A2434.